PROCEEDINGS, 50th Workshop on Geothermal Reservoir Engineering
Stanford University, Stanford, California, February 10-12, 2025
SGP-TR-229

Fast Marching Method: A New Paradigm for Rapid Simulation of Enhanced Geothermal Systems

Chin-Hsiang Chan, Akhil Datta-Gupta and Roman J. Shor

Texas A&M University, College Station, TX, USA

keisyo@tamu.edu

Keywords: enhanced geothermal system, reduced order model, rapid thermal output forecast

ABSTRACT

The Enhanced Geothermal System (EGS) allows access to heat energy stored in hot and dry rock, inaccessible to production via traditional hydrothermal systems. The EGS is expected to significantly contribute to a sustainable energy future. However, a key challenge in geothermal resource development is predicting the flow rate, temperature and thermal output of the produced subsurface fluid. One of the preferred methods for such forecasting is the reservoir simulation which is widely used in the oil and gas industry for predicting subsurface fluid production. EGS reservoir simulations involve complex physics, including non-isothermal, compositional flow within hard rocks containing hydraulic and natural fractures. These simulations are computationally intensive, often requiring several hours to days to complete a single simulation run. In this work, we propose a new paradigm for rapid multi-domain, multi-resolution simulation of EGS that accelerates reservoir simulation by orders of magnitude.

Our reservoir simulation method uses a finite-volume-based Fast Marching Method (FMM) to efficiently compute Diffusive Time of Flight (DTOF) and transform 3D simulations into equivalent 1D simulations using DTOF as spatial coordinate. The DTOF, which tracks pressure front propagation, guides the discretization of the 1D mesh. To maintain accuracy, the proposed method preserves 3D resolution near the wellbore and hydraulic fractures while converting the rest of the reservoir to 1D grid, resulting in significant computational speed up. The 3D and 1D domains communicate through non-neighbor connections that incorporate both fluid and heat transmissibility. Our proposed method was applied to a triplet horizontal well model consisting of one horizontal injector located between two horizontal producers for efficient heat extraction. Cool water is injected into the reservoir through the injector, and heated fluids are extracted from the producers. We performed reservoir simulations for 20 years to evaluate the life-scale performance of geothermal projects. The proposed FMM based multi-resolution simulation model provides flow rates, temperature and thermal power output with orders of magnitude speed up compared to full 3D fine-scale simulation. With the accelerated workflow, the proposed approach now allows for performance assessment and optimization of geothermal projects in hours compared to the typical timeframe of several days using commercial simulators, making such modeling practically feasible for routine applications.

1. INTRODUCTION

Geothermal energy, a form of thermal energy stored within Earth's subsurface, originates from heat accumulated over millions of years. This energy arises due to a significant thermal gradient between the Earth's hot core and its relatively cooler surface. This gradient facilitates the upward transfer of heat, making geothermal energy a sustainable resource for power generation in regions with favorable geological conditions (Gupta & Roy, 2007). Geothermal energy currently has an installed electric capacity of 15 GW worldwide and is expected to increase to 126 GW to align with Net Zero emission goals by 2050, according to the International Energy Agency's (IEA) scenario (IEA, 2021), as shown in Figure 1 (a). Traditional hydrothermal systems require the presence of natural aquifer with high reservoir permeability formation for efficient extraction of thermal energy. However, such systems are geographically constrained, as they rely on specific subsurface conditions that are not widely distributed. In contrast, high-enthalpy geothermal resources stored in low-permeability hot dry rock (HDR) have gained significant attention due to their excellent and sustainable potential for broader application (Esteves et al., 2019). For extracting heat energy from HDR, Enhanced Geothermal System (EGS) was initially proposed at the Los Alamos National Laboratory in the USA and has been widely studied in recent years (Olasolo et al., 2016). Figure 1 (b) illustrates typical EGS reservoir which involves both injector and producer drilled in low permeability HDR formation. Cool water is injected through injector and extracted from producer absorbing subsurface heat energy. Typically, the reservoir is stimulated to create enough hydraulic connections between injector and producer. Multiple enhanced geothermal pilot projects have been conducted to date, including the Utah FORGE (Frontier Observatory for Research in Geothermal Energy) Project (Moore & McLennan, 2018) and Fervo Energy's project in northern Nevada (Norbeck & Latimer, 2023).

The key uncertainties regarding geothermal resources are fluid production rate and its temperature. Both temperature and reservoir pressure may decrease over time as the supplemented heat travels increasingly longer distances to reach the wellbore. Various methods are used to predict these geothermal production performances. Decades ago, decline curve analysis was used to predict future production performance (Ripperda & Bodvarsson, 1987). Recently, one dimensional modeling discretizing the fracture plane with 1D mesh is utilized (Ricks et al., 2024). However, this simplified model is limited in its ability to account for the heat energy contributions from the reservoir matrix. One of the preferred methods for forecasting geothermal performance is 3D reservoir simulation, a methodology widely adopted in the oil and gas industry for predicting subsurface fluid production. This high-fidelity fractured reservoir modeling begins with a static geological model for the reservoir matrix, followed by the simulation of fracture propagation. Based on the results of fracture propagation

simulations, the matrix model is transformed into a reservoir model that incorporates matrix-fracture interactions, which is typically represented using an unstructured grid, a dual continuum approach, or an embedded discrete fracture model (EDFM).

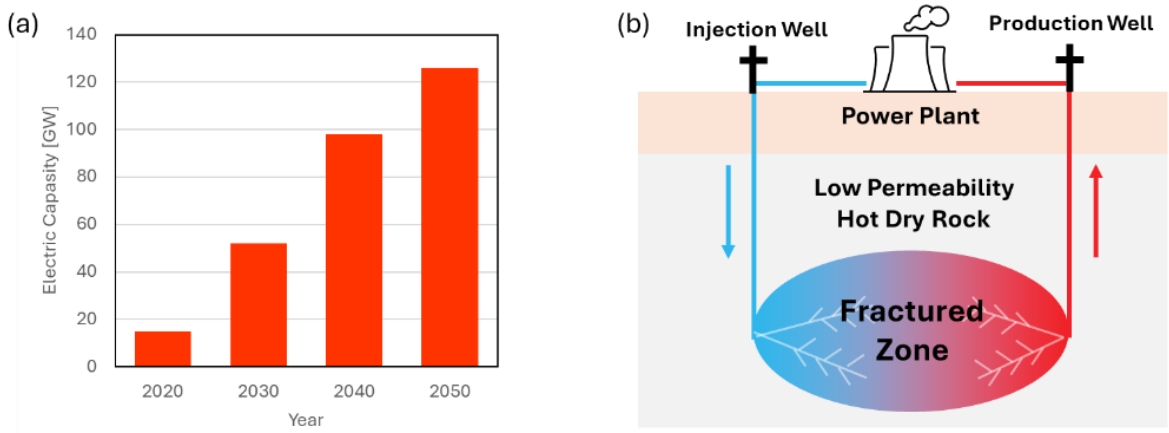

Figure 1: (a) Expected worldwide geothermal energy supply. Figure is created based on IEA (2021). (b) Schematic of enhanced geothermal system

Several studies in the literature have already utilized 3D reservoir models to simulate the performance of geothermal reservoirs (Shi et al., 2019; Xie et al., 2022). These geothermal reservoir simulations involve complex physics including non-isothermal, compositional flow within complex fracture-matrix media. Accurately simulating these physics requires significant computational resources, which limits finer scale grid or more complex fracture representation. For accelerated reservoir simulation, Fast Marchin Method (FMM)-based rapid simulation has been widely applied to unconventional reservoirs (Chen et al., 2023; Fu et al., 2024; Zhang et al., 2016). This method uses a finite-volume-based FMM (Chen et al., 2021) to efficiently compute Diffusive Time of Flight (DTOF) and transform 3D simulations into an equivalent multi-resolution simulation using DTOF as spatial coordinate. The DTOF, which tracks pressure front propagation (Datta-Gupta et al., 2011), guides the discretization of the 1D mesh. To maintain accuracy, the proposed method preserves 3D resolution near the wellbore and hydraulic fractures while converting the rest of the reservoir to 1D grid, resulting in significant computational speed up. The 3D and 1D domains communicate through non-neighbor connections (NNCs). This method achieves acceleration by orders of magnitude in reservoir simulations. The primary assumption in this FMM-based simulation is that the pressure contours coincide with the DTOF contours, a premise that is justified in most unconventional reservoir applications with low permeabilities where the pressure transients persist for a long time. EGS reservoirs share similar properties with unconventional reservoirs, particularly in their low permeability, and transient pressure regime throughout the operational period of EGS reservoirs. This similarity suggests that our FMM-based simulation can be effectively applied to EGS reservoirs. The objective of this work is to extend the FMM-based simulation to geothermal application and accelerate the reservoir simulation by orders of magnitude.

This paper is structured as follows. The *Introduction* section provides an overview of geothermal energy, establishing the foundational background for the research. The *Methodology* section then elaborates on the proposed methods in detail. Following this, the *Application* section presents both synthetic and field-scale case studies to demonstrate the practical applicability of the proposed methods. This paper concludes with a *Conclusion* section, summarizing key findings and implications.

2. METHODOLGY

A rapid reservoir simulation method using a coordinate transformation from the 3D physical space to the 1D DTOF contour space was proposed (Zhang et al., 2016) and applied to various reservoir conditions including multi-phase, multi-component flow (Fujita et al., 2016; Iino et al., 2020), non-isothermal flow with fracture (Cui et al., 2016; Zhang & Zhu, 2020), flow considering gravity (Onishi et al., 2019), coupled flow and geomechanics model (Terada et al., 2023). Our proposed rapid reservoir simulation method is based on the finite-volume FMM-based simulation proposed by Chen et al. (2023). This approach transforms a full 3D fine-scale model to an equivalent multi-resolution model using DTOF as spatial coordinate.

2.1 Diffusive Time of Flight (DTOF)

DTOF represents the contours of peak arrival time of pressure front propagation corresponding to an impulse source. This variable is derived from analogies between pressure propagation and wave propagation. First, we start with the diffusivity equation for fluid flow in heterogeneous permeable media.

$$\phi(\mathbf{x})\mu c_t \frac{\partial P(\mathbf{x},t)}{\partial t} = \nabla \cdot [k(\mathbf{x})\nabla P(\mathbf{x},t)] \tag{1}$$

where $\mathbf{x}$ is the spatial variable, t is time, ϕ is reservoir porosity, μ is fluid viscosity, c_t is total compressibility, P is pressure, k is reservoir permeability. Applying Fourier transform (Eq.2) to Eq. 1 gives the pressure in the frequency domain $\tilde{P}$.

$$\tilde{P}(\mathbf{x},\omega) = \int_{-\infty}^{\infty} P(\mathbf{x},t)e^{-i\omega t}dt \tag{2}$$

$$\phi(\mathbf{x})\mu c_t(-i\omega)\tilde{P}(\mathbf{x},\omega) = \nabla k(\mathbf{x})\cdot\nabla\tilde{P}(\mathbf{x},\omega) + k(\mathbf{x})\cdot\nabla^2\tilde{P}(\mathbf{x},\omega) \tag{3}$$

where ω is the frequency variable. An asymptotic approach is utilized to find a solution to Eq. 3 based on the asymptotic ray theory. This method has proven effective for analyzing front propagation in general (Sethian, 1996). Based on previous work in diffusive electromagnetic imaging and hydrology (Datta-Gupta et al., 2001; Vasco et al., 2000; Virieux et al., 1994), the asymptotic pressure solution is expressed as an infinite series as below.

$$\tilde{P}(\mathbf{x},\omega) = \exp\left[-\sqrt{-i\omega}\tau(\mathbf{x})\right]\sum_{k=0}^{\infty}\frac{A_k(\mathbf{x})}{\left(\sqrt{-i\omega}\right)^k} \tag{4}$$

where $\tau(\mathbf{x})$ represents the phase of a propagating wave and thus, describes the geometry of a propagation front, and we call this variable τ as DTOF. $A_k(\mathbf{x})$ are real functions that relate to the amplitude of the wave. The motivation for utilizing a solution expressed in inverse powers of ω lies in the high-frequency limit, where the leading terms of the series dominate. These initial terms encapsulate the rapidly oscillating components of the solution and effectively model the propagation of a sharp front. Consequently, essential physical quantities are captured within just the first few terms, providing a concise yet accurate representation of the system's behavior. Focusing on the leading-order term (k=0), substituting Eq. 4 with k=0 into Eq. 3 and solving for imaginary part provides following equation (Chen et al., 2021).

$$\nabla^{\mathrm{T}}\tau(\mathbf{x})\cdot\vec{k}(\mathbf{x})\cdot\nabla\tau(\mathbf{x}) = \phi(\mathbf{x})\mu c_t \tag{5}$$

where $\vec{k}$ represents the permeability tensor. Eq. 5 represents the form of the well-known Eikonal equation, which accounts for a wide range of propagation behaviors. This Eikonal equation has been extended for multi-phase flow (Fujita et al., 2016) and connection-based formulation (Chen et al., 2021) as below.

$$\sum_{m(n)}^{\tau_m<\tau_n} T_{nm}\cdot(\tau_n-\tau_m)^2 = \mu c_t V_{p,n} \tag{6}$$

where T_{nm} is transmissibility between cell n and m, τ_n is DTOF at cell n, $V_{p,n}$ is pore volume of cell n. The notation of $\tau_m < \tau_n$ indicates only upstream cells are considered and $m(n)$ indicates connections of cell n. In other words, only upstream connections are considered in Eq. 6. Since the DTOF value of a grid block depends solely on the DTOF values of upstream blocks, the solution can be systematically constructed from lower to higher values. Such strategy is developed as a numerical algorithm called the Fast Marching Method (FMM) by Sethian (1999). Utilizing FMM, the Eikonal equation can be solved within a few seconds for millions of grid cells.

The correlation between the pressure front and DTOF has been well investigated in the literature, including studies on pressure change versus DTOF (Wang et al., 2024), the time derivative of pressure change versus DTOF (Li et al., 2021), and the time derivative of pressure change versus exponential term of DTOF, $\exp(-\tau^2/4t)$ (King et al., 2016). These results show excellent agreement between pressure change and DTOF in reservoirs with low heterogeneity, while higher heterogeneity introduces more scatter but preserves the overall trend. The limitation of DTOF is that this variable cannot account for boundary effects without special treatment. Nakajima and King (2021) and Terada et al. (2024) demonstrated that DTOF is unsuitable as a spatial grid for conventional reservoirs with high permeability, where the pressure front reaches the boundary in early period. They alternatively proposed using a Pseudo-Steady-State pressure solution as a pressure change contour, which yielded good results in calculating pressure changes for conventional reservoirs, including CCS applications (Terada et al., 2024). However, EGS reservoirs have low permeability, making the diffusion process dominant throughout the entire operation. Hence, we use DTOF as the spatial coordinate in this research.

2.2 Fast Marching Method-based Rapid Reservoir Simulation

2.2.1 General Simulation Workflow

Figure 2 shows the general workflow of FMM-based rapid multi-domain, multi-resolution reservoir simulation. Beginning with a fine-scale reservoir model, DTOF is first calculated using the FMM. Based on the contours of DTOF, cells are grouped to define multiple DTOF levels, where the volume enclosed by two pressure contours constitutes one level. The model is also divided into local and shared domains for multi-well applications. Local domain represents the drainage volume controlled by individual wells while shared domain controls the multi-well interference. A multi-resolution model is constructed by converting DTOF levels into 1D grids in terms of pore volumes enclosed by DTOF levels and transmissibilities between levels. Typically, the first few levels near the wellbore are preserved in the original fine-scale resolution in order to account for complex flow patterns near the wellbore and also gravity effects. Hence, the resulting model has a multi-resolution grid system, 3D grids near the wellbore and 1D grids for rest of the grid system. The preserved 3D grids and 1D grids are connected through non-neighbor connections (NNCs) with the outermost cells in the preserved domain connected to the first cell in the 1D domain. After the multi-resolution grid is defined, the properties and transmissibilities of the upscaled model are computed. Most properties are obtained by pore volume weighting of fine-scale grid values within individual levels. The transmissibility upscaling is described in next section.

The outcome of this approach is a multi-resolution simulation model that accelerates well performance calculations by several orders of magnitude with minimal loss of accuracy. The multi-resolution model is designed for compatibility with commercial simulators to utilize advanced numerical calculations. By significantly reducing number of active cells, computational time is minimized, while accuracy is maintained through preserving the fine-scale region near the wellbore. The size of the preserved fine-scale domain is user-defined, often defined by a preserve ratio. A preserve ratio is the percentage of grid cells in the preserved domain to the total number of grid cells. Smaller preserve ratio provides larger acceleration and larger preserve ratio provides more accurate estimation. Hence, there is a trade-off between accuracy and acceleration.

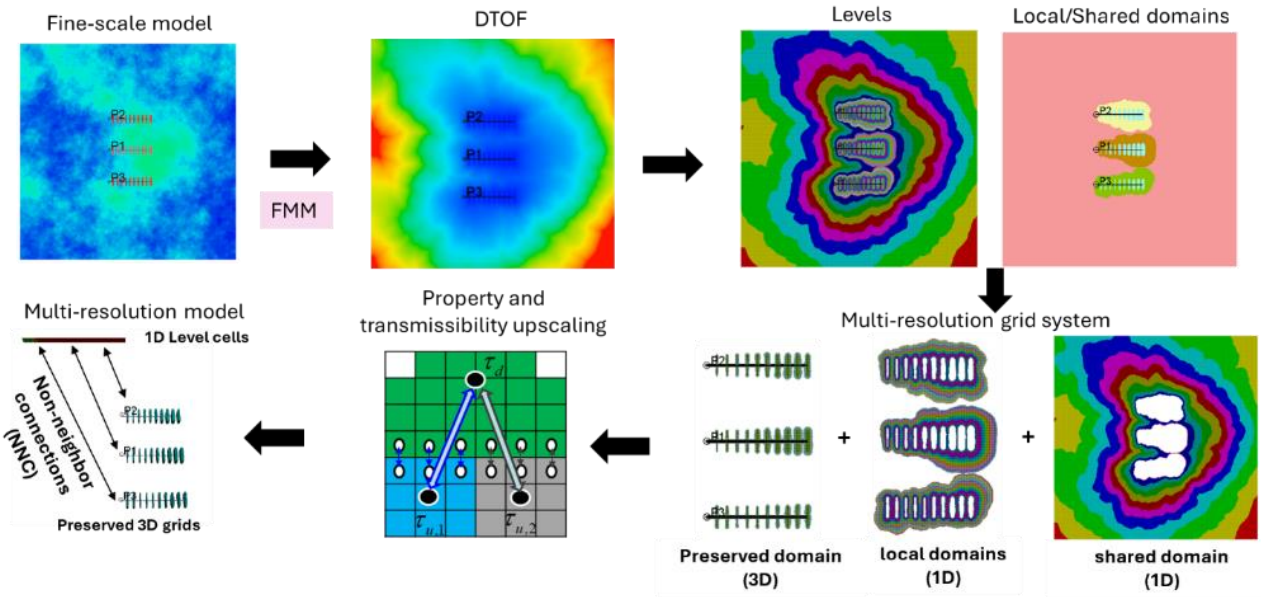

Figure 2: Multi-domain multi-resolution simulation workflow. This figure is adapted from Chen et al. (2023).

2.2.2 Transmissibility through Non-Neighbor Connections

The multi-resolution model involves many NNCs, as all outermost cells in the preserved domain are connected to a 1D domain. These NNCs involve two transmissibilities: one for fluid flow and another for heat flow. The fluid transmissibility in the upscaled model is computed based on the finite-volume-based Eikonal equation (Eq. 6). Reformulating Eq. 6 gives following equation for transmissibility (Chen et al, 2023).

$$T_{nm} = \frac{\mu c_t V_{p,n}}{(\tau_n - \tau_m)^2} \tag{7}$$

After defining the multi-resolution grid, upscaled cell properties are computed through pore volume weighting including for DTOF. Based on these upscaled cell properties and fluid properties, the transmissibility across upscaled cell is computed using Eq. 7.

In addition to the fluid transmissibility, another transmissibility is defined for heat flow. The transfer of heat within subsurface environments is predominantly governed by two primary mechanisms: convection and conduction. Convection involves the transport of heat via fluid movement, while conduction refers to the transfer of thermal energy through the solid medium without any material flow. The energy conservation equation is given as follows.

$$\frac{d}{dt}(V_b e) + F_e + C_e = 0 \tag{8}$$

where V_b is bulk volume, e is bulk internal energy density, F_e is convective enthalpy flow rate into neighboring grid blocks, and C_e is conductive energy flow rate into neighboring grid blocks. The convective enthalpy flow is defined as follows.

$$F_e = \sum_n T_{nm} \sum_p \left(h_p \cdot k_{rp}(S_p) \cdot \frac{b_p}{\mu_p} dP_{pnm} \right) \tag{9}$$

where subscript p indicates phase, h is molar enthalpy, k_r is relative permeability, S is saturation, b is molar density, and dP_{pnm} is potential difference of phase p between cells n and m. The convective enthalpy flow across the NNCs can be represented using the fluid transmissibility as shown in Eq. 9. The conductive energy flow is defined as follows.

$$C_e = -\sum_n H_{nm}\left(T_{temp,m} - T_{temp,n}\right) \tag{10}$$

where H is thermal conduction transmissibility and T_{temp} is temperature of the cell. In the following section, we will refer to this thermal conduction transmissibility simply as thermal transmissibility for the sake of simplicity. To accurately model thermal conduction transfer in the NNCs, it is essential to define the thermal transmissibility across the NNCs. We use the correlation between fluid and thermal transmissibility to compute the thermal transmissibility in the NNCs from fluid transmissibility computed through Eq. 7. Fluid transmissibility is computed as follows:

$$T_i = k_i \cdot \frac{A}{D_i}, \quad \frac{1}{T_{i\to j}} = \frac{1}{T_i} + \frac{1}{T_j} \tag{11}$$

The cell transmissibility T_i is computed from permeability, contact area A and distance between cell centers D_i. The intercell transmissibility $T_{i\to j}$ is computed through harmonic mean of connected cell transmissibilities. Similarly, the thermal transmissibility is defined as follows:

$$H_i = \kappa_i \cdot \frac{A}{D_i}, \quad \frac{1}{H_{i\to j}} = \frac{1}{H_i} + \frac{1}{H_j} \tag{12}$$

where κ is average cell thermal conductivity, which is computed from porosity weighted averaging of fluid and rock thermal conductivity. The only difference between fluid and thermal transmissibility is the use of thermal conductivity instead of permeability. We can express the correlation between two cell transmissibilities as follows.

$$H_i = \alpha_i \cdot T_i, \quad \alpha_i = \frac{\kappa_i}{k_i} \tag{13}$$

where α is thermal conversion factor which is a ratio of thermal conductivity to permeability. The intercell heat transmissibility is then computed from fluid transmissibilities as follows.

$$H_{i\to j} = \bar{\alpha}_{ij} \cdot T_{i\to j}, \quad \bar{\alpha}_{ij} = \frac{\alpha_i + \alpha_j}{2} \tag{14}$$

Eq. 14 assumes that thermal conversion factor in connected cell is approximately the same ($\alpha_i \approx \alpha_j$). This assumption should be valid, since the proposed multi-resolution gridding scheme preserves the region near wellbore and hydraulic fractures, where the high contrasted permeability is typically observed. Rest of reservoir have relatively low contrast properties, and this assumption will not cause large error in computation. Using Eqs.7 and 14, the fluid and thermal transmissibilities are computed and assigned to corresponding NNCs.

2.3 Embedded Discrete Fracture Model (EDFM) Considering Heat Flux

Modeling complex fracture systems is critical to predict fluid and heat flow in fractured reservoirs. The dual continuum model, first introduced by Warren and Root (1963), has been widely utilized for reservoir simulations with densely distributed, small-scale fractures or reservoirs with sparsely distributed large-scale fracture (Azom & Javadpour, 2012). The Discrete Fracture Network (DFN) model offers a more accurate representation of fluid flow within fractures and between the matrix and fractures, as the grid system is specifically designed to explicitly capture the fracture geometry. However, DFN comes with significant computational demands since it often requires an unstructured grid system, which introduce additional complexity to reservoir models (Cho et al., 2019). To balance the accuracy of DFN with the efficiency of the dual continuum model, the Embedded Discrete Fracture Model (EDFM) was proposed (Li & Lee, 2008). EDFM connects the discrete fractures to the matrix of a structured grid system by additional connection information (NNCs) and corresponding transmissibilities. Figure 3 shows an illustration of EDFM where the connections between matrix-fracture and fracture-fracture are represented by colored arrows.

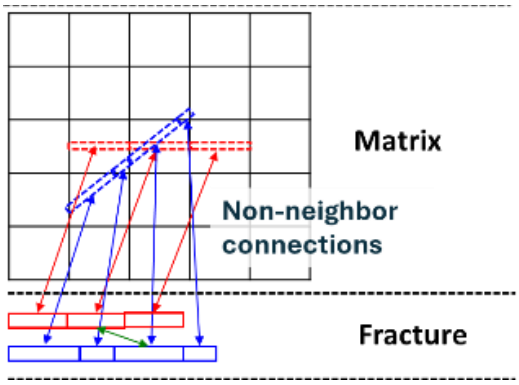

Figure 3: Illustration of EDFM

The transmissibility in these NNCs are computed using following equations (Moinfar et al., 2014).

$$\text{Fracture} - \text{Matrix: } \frac{A^{NNC}k^{NNC}}{d^{NNC}} = \frac{A\bar{k}_{mf}}{\langle d \rangle}, \quad \langle d \rangle = \frac{\int_V x_n \, dV}{V} \tag{15}$$

$$\text{Fracture} - \text{Fracture: } \frac{A^{NNC}k^{NNC}}{d^{NNC}} = \frac{wl_{int}\bar{k}_{ff}}{d_{ff}} \tag{16}$$

$$\text{Intersecting Fractures: } \frac{A^{NNC}k^{NNC}}{d^{NNC}} = \frac{T_1T_2}{T_1 + T_2}, \quad T_i = \frac{k_{fi}\omega_{fi}l_{int}}{d_{fi}} \tag{17}$$

where A is fracture surface area in the grid cell, k_{mf} is harmonic average of matrix and fracture permeabilities, and $\langle d \rangle$ is average normal distance. x_n is normal distance of the element from the fracture and V is volume of grid cell. T_i is transmissibility of each fracture, where d_{fi} is average of normal distances from the center of the fracture subsegments to the intersection line. Also, k_{fi} is fracture permeability, ω_{fi} is fracture aperture, and l_{int} is length of the intersection line. d_{ff} is distance between the centers of each fracture, and k_{ff} is harmonic average of fracture permeabilities.

To accurately model heat flow in the EDFM grid system, additional thermal transmissibilities need to be added to the NNCs to account for conductive thermal transfer. The thermal transmissibilities are defined in a similar manner where thermal conductivity is used instead of permeability.

$$\text{Fracture} - \text{Matrix: } \frac{A^{NNC}\kappa^{NNC}}{d^{NNC}} = \frac{A\bar{\kappa}_{mf}}{\langle d \rangle}, \quad \langle d \rangle = \frac{\int_V x_n \, dV}{V} \tag{18}$$

$$\text{Fracture} - \text{Fracture: } \frac{A^{NNC}\kappa^{NNC}}{d^{NNC}} = \frac{wl_{int}\bar{\kappa}_{ff}}{d_{ff}} \tag{19}$$

$$\text{Intersecting Fractures: } \frac{A^{NNC}\kappa^{NNC}}{d^{NNC}} = \frac{T_1T_2}{T_1 + T_2}, \quad T_i = \frac{\kappa_{fi}\omega_{fi}l_{int}}{d_{fi}} \tag{20}$$

3. SYNTHETIC EDFM CASE APPLICATION

The proposed FMM-based rapid simulation approach is first applied to a synthetic 3D EDFM case, which is illustrated in Figure 4. This model has gird dimension of 100 × 140 × 15, which is 0.2 million cells in total. The reservoir size spans 2,000 ft × 3,000 × 300 ft at a depth of 8,500 ft. This model has a triplet horizontal well system (Ricks et al., 2024), where a single horizontal injector is located between two horizontal producers. These wells are hydraulically connected through hydraulic fractures, initiated from the injector. Multi-stage hydraulic fracturing is performed with 3 stages and 4 clusters per stage. A single planar fracture is assumed to propagate from each cluster, thus there are 12 hydraulic fractures in total. The stage and cluster spacing are 100 ft. The fracture half-length is 200 ft, fracture height is 150 ft and fracture conductivity is 200 md-ft. The natural and induced fractures near the hydraulic fractures are modeled using the concept of stimulated reservoir volume (Mayerhofer et al., 2008), where relatively larger permeability is assigned to account for complex fracture network. This stimulated reservoir volume is typically designed to cover the region where microseismic activities are observed, and in this model, it covers the entire region containing the hydraulic fractures. The porosity field of reservoir matrix was generated using sequential Gaussian simulation, with values ranging from 0.0012 to 0.0101. The horizontal permeability field was then created using cokriging based on the porosity field, with permeability values ranging from 1.0×10^{-4} to 3.0×10^{-4} md. Vertical permeabilities were defined using a factor of 0.1 applied to the horizontal permeability values to account for permeability anisotropy. The rock heat capacity is 32.393 $\text{Btu/ft}^3/°\text{R}$. The rock and fluid thermal conductivities are 42.32 and 9.7132 Btu/ft/day/°R respectively. An industrial analytical formulation for water and steam properties is used for fluid properties (Wagner et al., 2000). Initial pressure and temperature are 2,900 psi and 400°F. Dirichlet boundary conditions are applied by assigning large pore and rock volumes to boundary cells to maintain constant pressure and temperature. We created the simulation deck using a commercial reservoir simulator, Eclipse Compositional Simulator (E300) with Thermal option to model non-isothermal, compositional simulation case. Cool water, at a temperature of 70°F, is injected through an injector with a controlled injection rate of 600 STB/day. Two producers maintain a BHP of 2,700 psi to extract fluid with thermal energy. The reservoir simulation is conducted over a 20-year period to evaluate the long-term geothermal performance of this model.

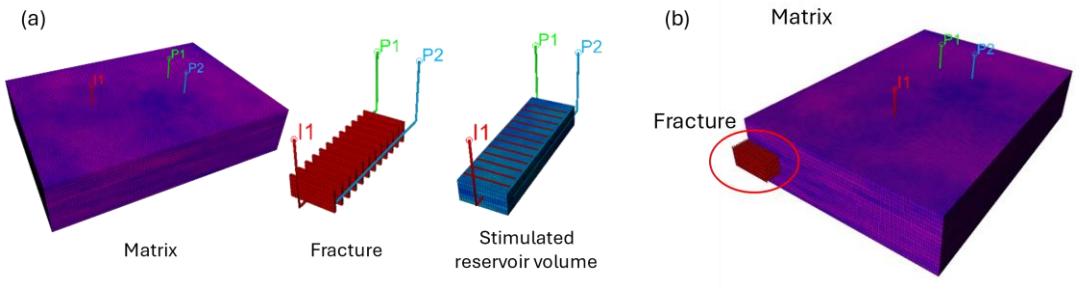

Figure 4: Synthetic EDFM case, (a) matrix, fracture and stimulated reservoir volume, and (b) converted EDFM grid where the region encircled in red represents the converted fractures

Figure 5 presents the results of the reservoir simulation after 20 years of operation. The top figures illustrate the dynamic reservoir properties, including distributions of reservoir pressure and temperature, with additional details for the fracture plane. Gravitational effects are observed in the fracture plane, with the upper sections experiencing lower pressure levels. Figure 5 (b) shows an apparent temperature reduction in the stimulated zone. Figure 5 (c)-(e) display the well performances of two production wells. The production fluid temperatures gradually decline from the initial reservoir temperature of 400°F because of the continuous injection of cool water. After 20 years, fluid temperatures have decreased by 28% and 21% for producers 1 and 2, respectively, relative to the initial temperature. The production rates for both wells remain stable, with a voidage replacement ratio (the ratio of the total volume of fluids injected to the volume of fluids produced) close to 100%, indicating minimal fluid loss due to the fully connected fractures between the injector and producers in the model. Figure 5 (e) illustrates the output thermal power of two producers, which quantifies the thermal energy produced from reservoir. This thermal output can be quantified using the following formula:

$$W_{pro} = m_{pro}\left(C_{p,pro}T_{temp,pro} - C_{p,inj}T_{temp,inj}\right) \tag{21}$$

where W_{pro} is production thermal power, $C_{p,m}$ is fluid heat capacity, m_{pro} is production mass rate and $T_{temp,m}$ is fluid temperature. As time progresses, the output thermal power gradually decreases, primarily due to the reduction in produced fluid temperature.

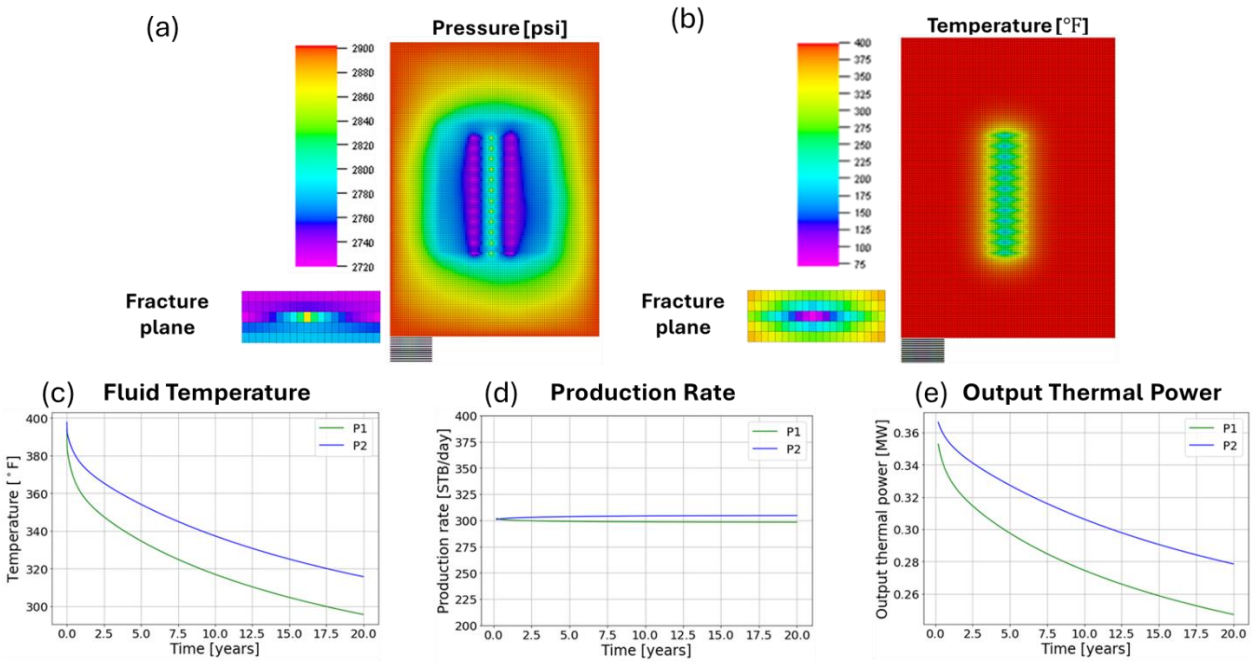

Figure 5: Reservoir dynamic properties and well performance of synthetic EDFM case: (a) reservoir pressure, (b) reservoir temperature, (c) production fluid temperature, (d) production rate and (e) output thermal power

The FMM-based rapid reservoir simulation is then applied to this synthetic EDFM case. The DTOF is computed using FMM, taking only 0.224 seconds. Using the DTOF contours, the multi-resolution model is constructed as illustrated in Figure 6 (a). Based on the contours of DTOF, the model is segmented into multiple levels. The first level is maintained at its original full 3D scale to capture near-wellbore physics, such as gravitational effects, while the remaining levels are transformed into equivalent 1D grids. Additionally, the model is divided into local and shared domains. However, in the EGS reservoir, local domains are small since hydraulic fractures connect the wells. Consequently, we focus primarily on the shared domain to determine the extent of the preserved region. The size of this preserved region

is defined by the "preserve ratio," representing the fraction of active cells retained. We explore multi-resolution models with 5%, 10%, and 15% preserve ratios to balance the trade-off between geothermal performance estimation accuracy and computational acceleration in reservoir simulation.

Figure 6 (b) presents a comparison of thermal performance across different models. The black solid line denotes the output thermal power of the full 3D fine-scale model, while the red, blue, and green dashed lines represent the thermal outputs of the multi-resolution models. Figure 6 (c) illustrates the preserved domain for each multi-resolution model. Notably, the model with a 15% preserved domain (red dashed line) provides thermal power most closely aligned with that of the fine-scale simulation. As the preserve ratio decreases, the thermal power progressively deviates from that of the fine-scale model, with general overestimation of thermal power in early time and underestimation of thermal power in late time. Table 7 summarizes computational performance and error of multi-resolution models against fine-scale simulation results. All simulations in this paper were conducted using an Intel® Xeon® CPU E5-2630 v4 with a base clock speed of 2.20 GHz and 32 GB RAM. While the full 3D fine-scale model requires around 3.62 hours for single reservoir simulation, the multi-resolution models require less than half of an hour. The 5% and 10% preserved models achieve more than an order-of-magnitude acceleration. This acceleration is primarily attributed to the substantial reduction in the number of active cells, which, in turn, decreases the number of primary variables required for the numerical calculation in reservoir simulation. This reduction decreases the computational load required for matrix calculations and improves convergence efficiency in Newton iterations. Additionally, the average relative error over time is computed for each model and presented in Table 7, revealing that the error remains within a few percent. FMM-based simulation effectively accelerates the reservoir simulations by more than an order of magnitude while maintaining a reasonable degree of accuracy.

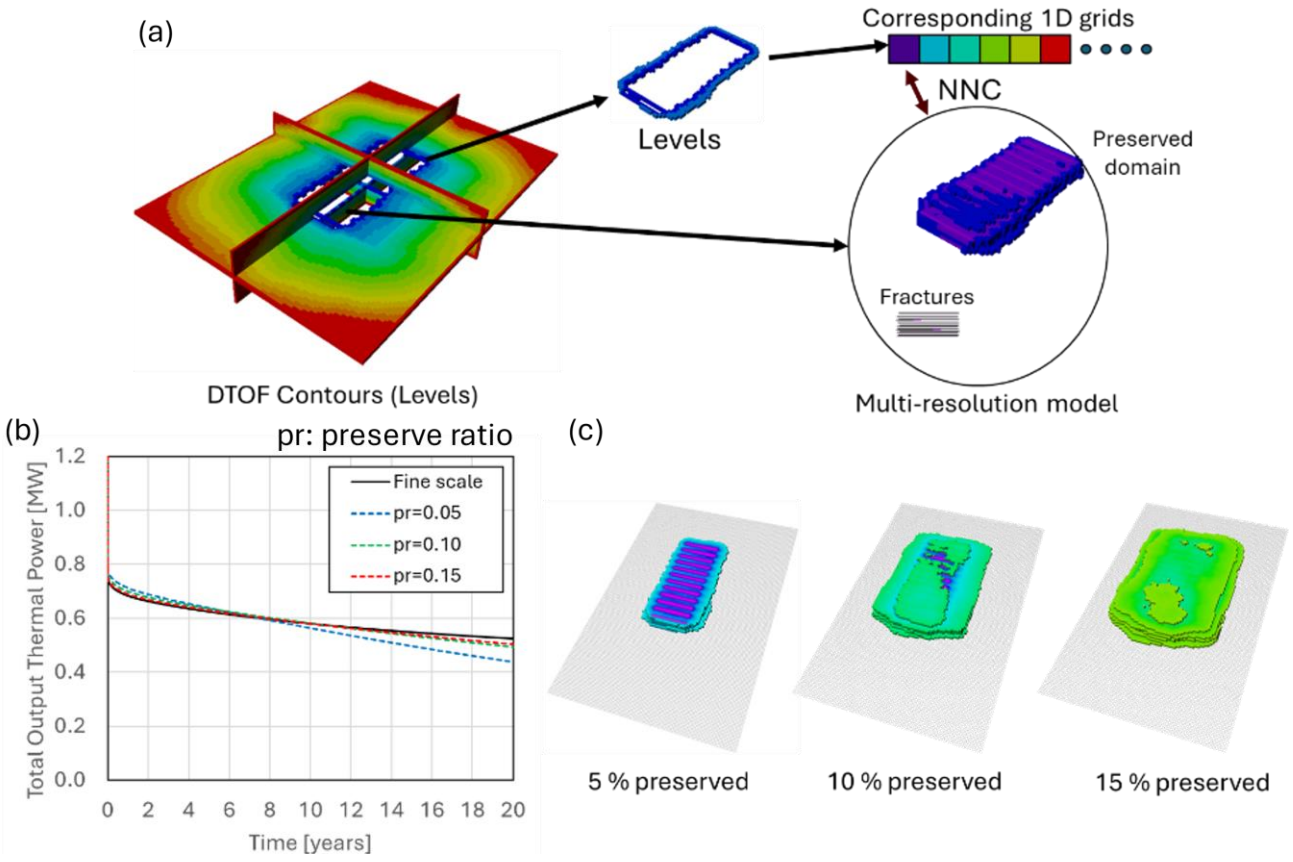

Figure 6: (a) Construction of multi-resolution model, (b) comparison of well performance, (c) preserved domain of 5, 10, 15 % preserved model

Table 7: Computational performance and error of multi-resolution models

Preserve ratio [%]	Required CPU time [min]	Acceleration [-]	Relative error [%]
5	14.4	15.1	6.32
10	17.2	12.6	2.25
15	28.0	7.7	1.30

4. FIELD-SCALE APPLICATION

4.1 Model Description and Construction of Multi-resolution Model

In this section, the proposed FMM-based rapid simulation is applied to a field-scale model with complex fractures. Figure 8 illustrates the field-scale fractured reservoir model developed using a commercial fracture propagation software with model parameters based on an Eagle Ford shale reservoir (Yang et al., 2017). The fracture propagation is simulated accounting for stress shadow effects and the interaction between hydraulic and natural fractures, resulting in a high-fidelity, non-planar, and complex fracture network. This model comprises of 400×560×7 grid blocks, totaling 1.56 million cells. It simulates a multi-stage hydraulic fracturing treatment with 100 ft spacing between fractures-clusters, resulting in a total of 20 evenly spaced non-planar fractures. Each fracture has heterogeneous permeability, with an average fracture conductivity of approximately 300 md-ft, and fracture half-lengths ranging from 50 to 330 ft. Initial conditions include a reservoir pressure of 2,900 psi and a temperature of 400°F. Fluid properties and thermal-related properties are same as in the previous synthetic case. The injection well is operated at an injection rate of 2,000 STB/day with 70°F cool water, while production wells are controlled by BHP of 2,175 psi. The reservoir simulation is conducted for a 20-year period.

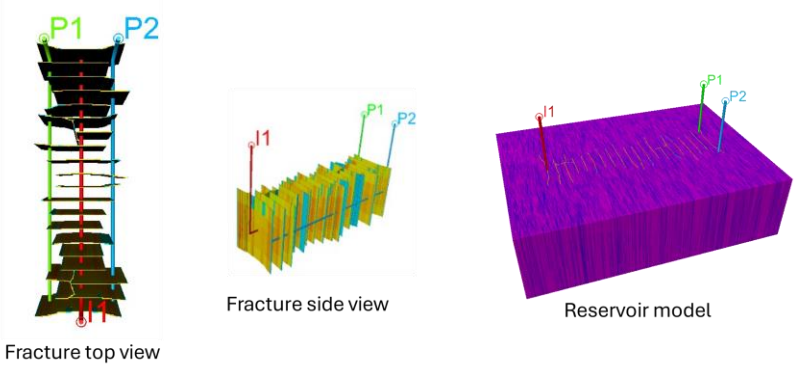

Figure 8: Field-scale complex fractured model

Figure 9 shows the reservoir simulation results including reservoir dynamic properties and well performance. The production wells only partially penetrate the fractures, causing pressure to increase in those fractures that lack a direct connection to producers as shown in Figure 9 (a). Injected fluid flows through connected hydraulic fractures, leading to a noticeable temperature reduction in these fractures in Figure 9 (b). The temperature of the produced fluid decreases by approximately 35% to 40% after 20 years. The temperature reduction primarily occurs during the first 10 years, after which it remains relatively stable. Due to incomplete fracture-producer connections, a fluid loss of around 4% of the injected volume is observed.

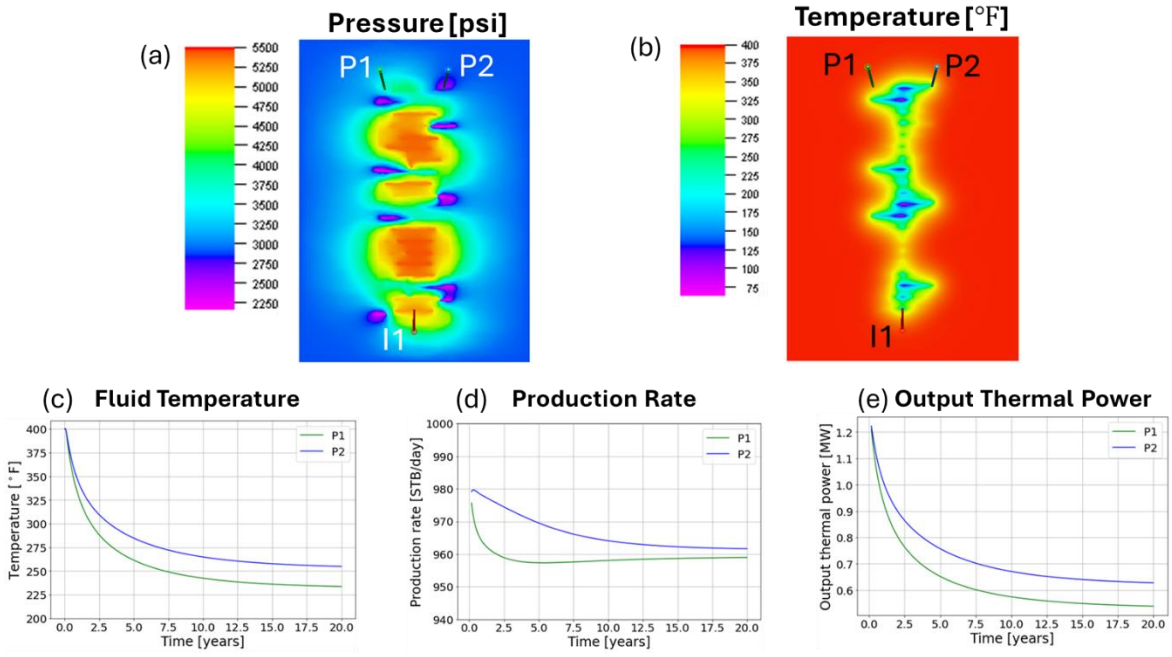

Figure 9: Reservoir dynamic properties and well performance in field-scale fractured model: (a) reservoir pressure, (b) reservoir temperature, (c) production fluid temperature, (d) production rate and (e) output thermal power

DTOF is computed in 2.8 seconds using FMM. Based on the DTOF contours, a multi-resolution model is constructed. Figure 10 presents the construction of multi-resolution model with different preserve ratio, and Table 11 summarizes their computational performance and associated errors. Notably, the model with a 15% preserve ratio demonstrates satisfactory performance, while the other two models exhibit larger errors, primarily due to differences between DTOF contours and temperature propagation. The proposed FMM-based simulation accounts for heat flow in the multi-resolution model. However, the conversion to 1D grids is based on DTOF contours, which are aligned with pressure contours. In EGS, the propagation of temperature exhibits distinct behaviors compared to pressure. Temperature changes in EGS are driven by two main factors: (1) temperature reduction due to energy depletion caused by fluid extraction and (2) temperature reduction induced by the injection of cool water. The temperature distribution related to the first factor is well captured by DTOF contours, while the second factor is not. To mitigate errors from this second factor, it is necessary to preserve regions affected by the cool water injection. However, the cooling effect from this second factor propagates more slowly and over a limited area, requiring only a small, preserved region. Thus, DTOF-based coordinate transformation still maintains reasonable accuracy while it provides more than an order of acceleration. A detailed investigation of these two mechanisms of temperature reduction and their correlation to DTOF is provided in the Appendix A.

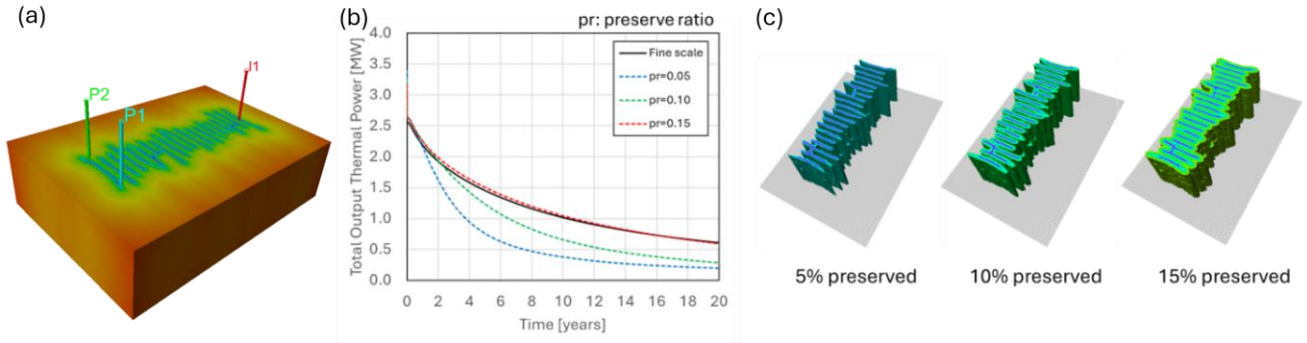

Figure 10: (a) DTOF in field-scale fractured model, (b) comparison of well performance in field-scale fractured model and (c) corresponding preserved grids of 5, 10, 15 % preserved model

Table 11: Computational performance and error of multi-resolution models in field-scale fractured model

Preserve ratio [%]	Required CPU time [hr]	Acceleration [-]	Relative error [%]
5	0.6	66.7	55
10	1.13	35.5	32
15	1.67	24.2	2.4

4.2 Rapid Simulation Studies

The proposed FMM-based simulation approach offers accelerated reservoir simulation, enabling a comprehensive analysis of development and operations in EGS reservoirs. Using the multi-resolution model, simulation studies are conducted leveraging more than an order of magnitude acceleration.

4.2.1 Well Spacing Analysis

The well spacing size between injector and producer is a key parameter in the EGS model. Smaller well spacing leads to a faster thermal circuit, while larger well spacing results in poor hydraulic connections between wells. The well spacing is changed between 50 to 300 ft to investigate the effect to the geothermal performance. Using 15% preserved model, simulation studies are conducted, and results are presented in Figure 12. Figure 12 (a) illustrates the relation between cumulative thermal power and well spacing. This analysis reveals that the optimal well spacing for maximizing thermal power is 150 ft. This computation is completed within 8 hours using the FMM-based simulation while a fine-scale simulation would require approximately 10 days, as shown in Figure 12 (b). Figure 12 (c) and (d) show the produced fluid temperature against time and cumulative fluid production from the models with different well spacing. The general trend indicates that as the well spacing increases, the temperature reduction becomes more gradual. One observation is that the model with a well spacing of 250 ft exhibits a sharper temperature reduction in the early period compared to the 200 ft well spacing model. This could be due to the fact that with larger well spacing, fewer fractures are connected between the injector and producer, causing the majority of the fluid to be concentrated in those connected fractures and resulting in faster thermal energy extraction near them. However, as shown in Figure 12 (d), larger well spacing leads to weaker hydraulic connectivity between the wells. As a result of the lower production rates, the produced fluid temperature in the 250 ft well spacing model is higher during the later period compared to the 200 ft well spacing model.

Figure 12 (e) shows the well layouts of three different well spacing sizes, where it is evident that the model with larger well spacing has fewer fracture connections with producers. Figure 12 (f) presents the temperature and production contribution profiles along the producers after 20 years of operation. The 50 ft well spacing model demonstrates a more uniform temperature reduction across nearly all well sections, whereas the other two models exhibit temperature reduction in only specific sections, where fractures have penetrated. The production contribution profile further supports this observation. The 50 ft well spacing model exhibits a more evenly distributed fluid contribution, whereas the 300 ft well spacing model shows production contributions in only a few sections. Additionally, focusing on the fluid production contribution from the first section near the heel, a larger contribution is observed with larger well spacing, suggesting more rapid thermal energy extraction in that section. However, the larger well spacing also results in greater contact with the geothermal system, leading to a more gradual temperature reduction.

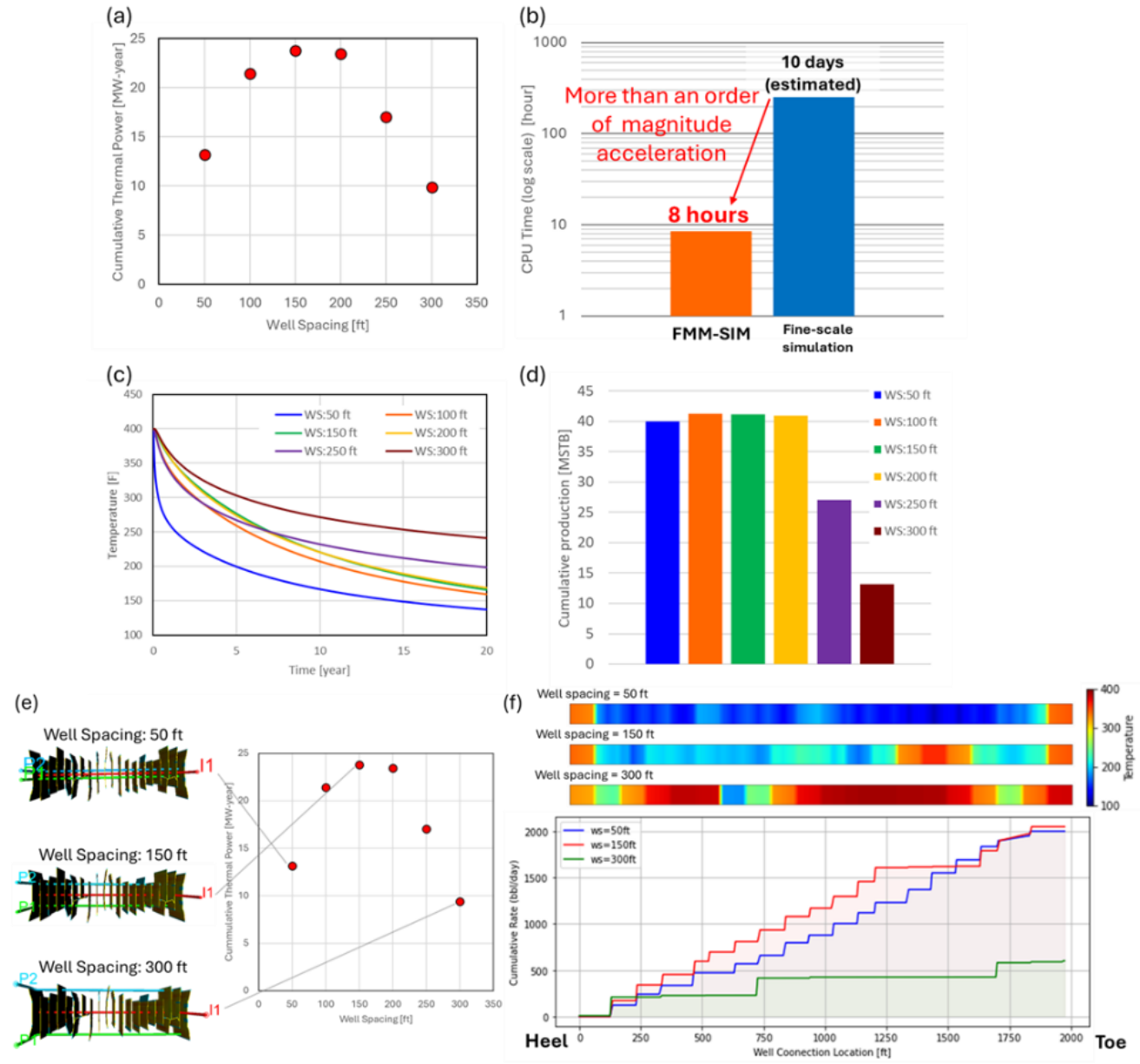

Figure 12: Results of simulation studies in well spacing analysis, (a) cumulative thermal power, (b) required CPU time, (c) produced fluid temperature, (d) cumulative production, (e) well layouts with different well spacings, and (f) temperature profiles and fluid production contribution along producers after 20 years

4.2.2 Water Injection Rates and Temperatures

Next, the impacts of water injection rates and temperatures are examined. Higher injection rate results in increased production while it leads to a faster temperature reduction. It should be noted that higher injection rates can cause higher BHP, which may potentially induce seismic activities. The 150 ft well spacing model is selected in this simulation study, as it provides the highest thermal power according to the previous investigation. Injection rates are varied from 1,000 to 4,000 STB/day, in increments of 500 STB/day with BHP constraints

of 4500 psi. The temperature is adjusted from 70°F to 120°F, with a 10°F difference between each setting. Figure 13 summarizes the results of this simulation study. Injecting more water increases cumulative production but also facilitates temperature reduction. Consequently, the relationship between the injection rate and thermal output is nonlinear. At injection rates exceeding 3,000 STB/day, the simulation encounters BHP limits, thereby restricting injection rates. Additionally, it is important to note that there is a specific threshold for production fluid temperatures required to economically generate electricity in a surface power plant. Once the temperature falls below this threshold, the reservoir no longer produces economically viable geothermal resources.

Figure 13 (b) shows the simulation results for different injection fluid temperatures. As the injected fluid temperature increases, the resulting temperature reduction in the produced fluid is mitigated. Linear relationship between injected fluid temperature and cumulative thermal output is observed. Heating the injected fluid increases energy consumption at surface facilities, but it significantly extends the lifespan of geothermal assets. For example, suppose the temperature threshold for production fluid to enable economically viable power generation is 200°F, injecting fluid at 70°F results in a lifespan of approximately 13 years. In comparison, injecting fluid at 120°F extends the lifespan by an additional 7 years. The heating of injection fluid should be considered based on the required energy for heating and the expected energy gain from injecting heated fluid.

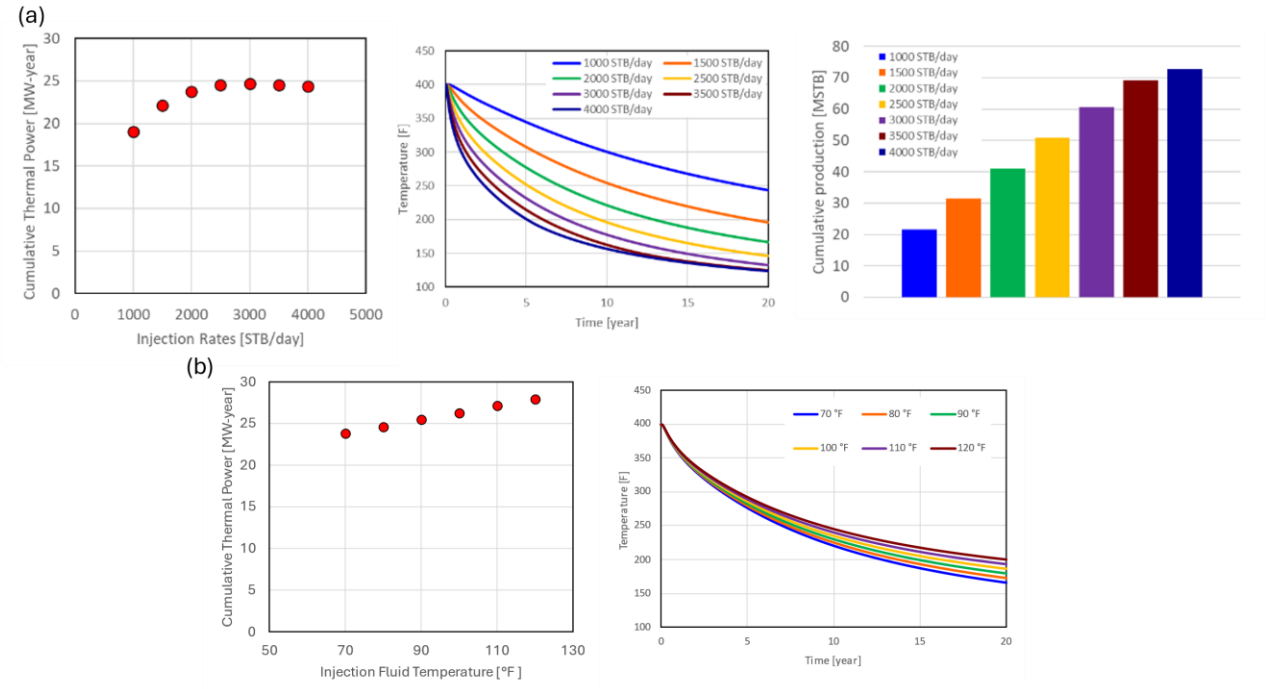

Figure 13: Results of simulation studies in (a) injection rates, (b) injection fluid temperature

5. CONCLUSION

In this paper, we presented an FMM-based reservoir simulation approach for geothermal application and demonstrated its application to rapid simulation studies in EGS reservoirs. The application of full 3D reservoir simulations for geothermal performance estimation is very often limited due to the excessive computational burden. Our proposed method enables accelerated high-fidelity reservoir simulations, which are expected to contribute to dynamic reservoir modeling through data assimilation or the optimization of development strategies that require numerous reservoir simulation runs. This paper presents the first application of FMM-based simulation for geothermal reservoir modelling. The acceleration of geothermal reservoir simulations is expected to play a pivotal role in the global implementation of geothermal energy, contributing significantly to achieving the Net Zero emission targets.

Our conclusions from this paper are summarized as follows:

- FMM-based simulation generates an equivalent multi-resolution simulation using the diffusive time of flight (DTOF) as spatial coordinate. This multi-resolution model offers more than an order of magnitude acceleration compared to full 3D fine-scale reservoir simulation with comparable accuracy. The DTOF is derived from the high-frequency limit of the asymptotic pressure solution to the diffusivity equation, representing the peak arrival time of the pressure front propagation. The DTOF gradients are closely aligned with the pressure gradients allowing us to convert 3D fine-scale model to equivalent multi-resolution model using DTOF as spatial coordinate.
- Our proposed method is first tested on a synthetic EDFM case, achieving an acceleration of more than an order of magnitude while maintaining sufficient accuracy (within 2-6% error). The trade-off between acceleration and accuracy was controlled through the fine-scale preserve ratio. Furthermore, we validated the applicability of the FMM-based simulation for high-fidelity fractured models and conducted rapid simulation studies, demonstrating the computational efficiency and practicality of the proposed approach.

- With the significant computational speed up, various scenarios were analyzed using the multi-resolution model, including the investigation of optimal well spacing and control strategies. Optimal well spacing was determined by factors such as heat transfer from the matrix to fractures and fluid flow from injectors to producers along hydraulic fractures. Optimal well control was investigated by changing injection rate and temperature.

REFERENCES

Azom, P. N., and Javadpour, F.: Dual-Continuum Modeling of Shale and Tight Gas Reservoirs, SPE Annual Technical Conference and Exhibition, San Antonio, Texas, USA (2012). https://doi.org/10.2118/159584-ms

Chen, H., Li, A., Terada, K., and Datta-Gupta, A.: Rapid Simulation of Unconventional Reservoirs by Multidomain Multiresolution Modeling Based on the Diffusive Time of Flight, *SPE Journal*, *28*(03), (2023), 1083-1096. https://doi.org/10.2118/214308-pa

Chen, H., Onishi, T., Park, J., and Datta-Gupta, A.: Computing Pressure Front Propagation Using the Diffusive-Time-of-Flight in Structured and Unstructured Grid Systems via the Fast-Marching Method, *SPE Journal*, *26*(03), (2021), 1366-1386. https://doi.org/10.2118/201771-pa

Cho, Y., Gibson, R. L., Lee, J., and Shin, C.: Linear-slip discrete fracture network model and multiscale seismic wave simulation, *Journal of Applied Geophysics*, *164*, (2019), 140-152. https://doi.org/https://doi.org/10.1016/j.jappgeo.2019.03.006

Cui, J., Yang, C., Zhu, D., and Datta-Gupta, A.: Fracture Diagnosis in Multiple-Stage-Stimulated Horizontal Well by Temperature Measurements With Fast Marching Method, *SPE Journal*, *21*(06), (2016), 2289-2300. https://doi.org/10.2118/174880-pa

Datta-Gupta, A., Kulkarni, K. N., Yoon, S., and Vasco, D.: Streamlines, ray tracing and production tomography: Generalization to compressible flow, *Petroleum Geoscience*, *7*, *SUPP*, *75*(86), (2001), 12.

Datta-Gupta, A., Xie, J., Gupta, N., King, M. J., and Lee, W. J.: Radius of Investigation and its Generalization to Unconventional Reservoirs, *Journal of Petroleum Technology*, *63*(07), (2011), 52-55. https://doi.org/10.2118/0711-0052-jpt

Esteves, A. F., Santos, F. M., and Magalhães Pires, J. C.: Carbon dioxide as geothermal working fluid: An overview, *Renewable and Sustainable Energy Reviews*, *114*, (2019), 109331. https://doi.org/https://doi.org/10.1016/j.rser.2019.109331

Fu, J., Chen, H., Yao, C., Sakaida, S., Kerr, E., Johnson, A., Datta-Gupta, A., Zhu, D., and Hill, A. D.: Field Application of a Novel Multiresolution Multiwell Unconventional Reservoir Simulation: History Matching and Parameter Identification, *SPE Journal*, (2024), 1-12. https://doi.org/10.2118/219444-pa

Fujita, Y., Datta-Gupta, A., and King, M. J.: A Comprehensive Reservoir Simulator for Unconventional Reservoirs That Is Based on the Fast Marching Method and Diffusive Time of Flight, *SPE Journal*, *21*(06), (2016), 2276-2288. https://doi.org/10.2118/173269-pa

Gupta, H., and Roy, S. Chapter 4 - GEOTHERMAL SYSTEMS AND RESOURCES. In H. Gupta & S. Roy (Eds.), *Geothermal Energy* (pp. 49-59). Elsevier. (2007). https://doi.org/https://doi.org/10.1016/B978-044452875-9/50004-6

IEA. (2021). *Net Zero by 2050*. IEA. https://www.iea.org/reports/net-zero-by-2050

Iino, A., Jung, H. Y., Onishi, T., and Datta-Gupta, A.: Rapid Simulation Accounting For Well Interference in Unconventional Reservoirs Using Fast Marching Method, SPE/AAPG/SEG Unconventional Resources Technology Conference, (2020). https://doi.org/10.15530/urtec-2020-2468

King, M. J., Wang, Z., and Datta-Gupta, A.: Asymptotic Solutions of the Diffusivity Equation and Their Applications, SPE Europec featured at 78th EAGE Conference and Exhibition, (2016). https://doi.org/10.2118/180149-ms

Li, C., Wang, Z., and King, M. J.: Transient drainage volume characterization and flow simulation in reservoir models using the fast marching method, *Computational Geosciences*, *25*(5), (2021), 1647-1666. https://doi.org/10.1007/s10596-021-10061-2

Li, L., and Lee, S. H.: Efficient field-scale simulation of black oil in a naturally fractured reservoir through discrete fracture networks and homogenized media, *SPE Reservoir evaluation & engineering*, *11*(04), (2008), 750-758.

Mayerhofer, M. J., Lolon, E. P., Warpinski, N. R., Cipolla, C. L., Walser, D., and Rightmire, C. M.: What is Stimulated Reservoir Volume (SRV)?, SPE Shale Gas Production Conference, (2008). https://doi.org/10.2118/119890-ms

Moinfar, A., Varavei, A., Sepehrnoori, K., and Johns, R. T.: Development of an efficient embedded discrete fracture model for 3D compositional reservoir simulation in fractured reservoirs, *SPE Journal*, *19*(02), (2014), 289-303.

Moore, J., and McLennan, J. D.: An Overview of the Utah Frontier Observatory for Research in Geothermal Energy (FORGE), AGU Fall Meeting Abstracts, (2018).

Nakajima, K., and King, M.: Development and Application of Fast Simulation Based on the PSS Pressure as a Spatial Coordinate, SPE Annual Technical Conference and Exhibition, (2021). https://doi.org/10.2118/206085-ms

Norbeck, J., and Latimer, T. (2023). Commercial-Scale Demonstration of a First-of-a-Kind Enhanced Geothermal System. X52X50B. Retrieved July 01, 2023, from https://ui.adsabs.harvard.edu/abs/2023EaArX...X52X0BN

Olasolo, P., Juárez, M. C., Morales, M. P., D´Amico, S., and Liarte, I. A.: Enhanced geothermal systems (EGS): A review, *Renewable and Sustainable Energy Reviews*, *56*, (2016), 133-144. https://doi.org/https://doi.org/10.1016/j.rser.2015.11.031

Onishi, T., Iino, A., Jung, H. Y., and Datta-Gupta, A.: Fast Marching Method Based Rapid Simulation Accounting for Gravity, SPE/AAPG/SEG Asia Pacific Unconventional Resources Technology Conference, (2019). https://doi.org/10.15530/ap-urtec-2019-198249

Ricks, W., Voller, K., Galban, G., Norbeck, J. H., and Jenkins, J. D.: The role of flexible geothermal power in decarbonized electricity systems, *Nature Energy*, (2024). https://doi.org/10.1038/s41560-023-01437-y

Ripperda, M., and Bodvarsson, G. S. (1987). *Decline curve analysis of production data from The Geysers geothermal field* Conference: 12. workshop on geothermal reservoir engineering, Stanford, CA, USA, United States. https://www.osti.gov/biblio/6662908

Sethian, J. A.: A fast marching level set method for monotonically advancing fronts, *Proceedings of the National Academy of Sciences*, *93*(4), (1996), 1591-1595. https://doi.org/doi:10.1073/pnas.93.4.1591

Sethian, J. A.: Fast Marching Methods, *SIAM Review*, *41*(2), (1999), 199-235. https://doi.org/10.1137/s0036144598347059

Shi, Y., Song, X., Wang, G., Li, J., Geng, L., and Li, X.: Numerical study on heat extraction performance of a multilateral-well enhanced geothermal system considering complex hydraulic and natural fractures, *Renewable Energy*, *141*, (2019), 950-963. https://doi.org/https://doi.org/10.1016/j.renene.2019.03.142

Terada, K., Chen, H., Iino, A., and Datta-Gupta, A.: Multi-Resolution Coupled Flow and Geomechanics Modeling Using Fast Marching Method, SPE/AAPG/SEG Unconventional Resources Technology Conference, (2023). https://doi.org/10.15530/urtec-2023-3859799

Terada, K., Datta-Gupta, A., and King, M. J. (2024). *Multi-Resolution Simulation for Efficient Pressure & Stress Calculation in Large-Scale CO2 Storage Using Pseudosteady State Pressure as Spatial Coordinate* Carbon Capture, Utilization, and Storage conference (CCUS), Houston. https://doi.org/10.15530/ccus-2024-4014878

Vasco, D. W., Keers, H., and Karasaki, K.: Estimation of reservoir properties using transient pressure data: An asymptotic approach, *Water Resources Research*, *36*(12), (2000), 3447-3465. https://doi.org/https://doi.org/10.1029/2000WR900179

Virieux, J., Flores-Luna, C., and Gibert, D.: Asymptotic Theory For Diffusive Electromagnetic Imaging, *Geophysical Journal International*, *119*(3), (1994), 857-868. https://doi.org/10.1111/j.1365-246X.1994.tb04022.x

Wagner, W., Cooper, J. R., Dittmann, A., Kijima, J., Kretzschmar, H. J., Kruse, A., Mareš, R., Oguchi, K., Sato, H., Stöcker, I., Šifner, O., Takaishi, Y., Tanishita, I., Trübenbach, J., and Willkommen, T.: The IAPWS Industrial Formulation 1997 for the Thermodynamic Properties of Water and Steam, *Journal of Engineering for Gas Turbines and Power*, *122*(1), (2000), 150-184. https://doi.org/10.1115/1.483186

Wang, Z., Li, C., and King, M. J.: Applications of Asymptotic Solutions of the Diffusivity Equation to Infinite Acting Pressure Transient Analysis, *SPE Journal*, *29*(08), (2024), 4069-4093. https://doi.org/10.2118/180149-pa

Warren, J. E., and Root, P. J.: The Behavior of Naturally Fractured Reservoirs, *Society of Petroleum Engineers Journal*, *3*(03), (1963), 245-255. https://doi.org/10.2118/426-pa

Xie, J., Wang, J., and Liu, X.: Performance analysis of pinnate horizontal well in enhanced geothermal system, *Applied Thermal Engineering*, *201*, (2022), 117799. https://doi.org/https://doi.org/10.1016/j.applthermaleng.2021.117799

Yang, C., Xue, X., King, M. J., and Datta-Gupta, A.: Flow Simulation of Complex Fracture Systems With Unstructured Grids Using the Fast Marching Method, SPE/AAPG/SEG Unconventional Resources Technology Conference, (2017). https://doi.org/10.15530/urtec-2017-2691393

Zhang, S., and Zhu, D.: Inversion of Downhole Temperature Measurements in Multistage-Fracturing Stimulation of Horizontal Wells in Unconventional Reservoirs, *SPE Production & Operations*, *35*(02), (2020), 231-244. https://doi.org/10.2118/187322-pa

Zhang, Y., Bansal, N., Fujita, Y., Datta-Gupta, A., King, M. J., and Sankaran, S.: From Streamlines to Fast Marching: Rapid Simulation and Performance Assessment of Shale-Gas Reservoirs by Use of Diffusive Time of Flight as a Spatial Coordinate, *SPE Journal*, *21*(05), (2016), 1883-1898. https://doi.org/10.2118/168997-pa

APPENDIX

Appendix A. Comparison of DTOF contours against temperature contour

DTOF has been well investigated in relation to pressure, while its application to temperature remains unexplored. To investigate the correlation between DTOF and temperature, a 2D synthetic model with a heterogeneous permeability field is used. This model features a single fracture at the center of the reservoir, with a single well also positioned at the center. There are two primary factors contributing to temperature reduction in EGS reservoirs: (1) temperature reduction due to energy depletion caused by fluid extraction and (2) temperature reduction induced by the injection of cool water. To analyze these two factors, two operational scenarios are investigated. The first scenario involves production from the centered well, while the second scenario involves injection from the centered well. This synthetic 2D model has an initial pressure of 2,900 psi, and in the first scenario, the well produces fluid with a BHP of 2,175 psi, causing temperature reduction due to energy depletion. In the second scenario, cool water at 50°F is injected instead of production, with the injector controlled by a BHP of 5,000 psi. This second scenario simulates the temperature reduction caused by cool water injection.

Figure A-1 shows a comparison of DTOF against temperature distributions in two scenarios. In the first scenario, DTOF correlates well with the temperature changes, whereas in the second scenario, this correlation is not observed. This discrepancy arises because energy depletion in the first scenario is driven by fluid extraction, which follows the same distribution as pressure, allowing DTOF to align well with temperature changes. In contrast, temperature reduction in the second scenario is primarily driven by the injection of cool water and is governed by heat conduction, which does not exhibit the same pressure-related distribution. In this case, the DTOF effectively captures only the first mechanism, since the temperature transfer is caused by a different mechanism. To account for the second effect, it is necessary to preserve the region where this effect occurs. However, as Figure A-1 illustrates, the temperature distribution in the second scenario is confined to a limited region, as the propagation is much slower compared to the first scenario. It is important to note that the simulation period of the first scenario is 1 year, while the second scenario is simulated over 20 years. Despite the longer simulation period in the second scenario, the temperature change does not propagate to a larger distance, suggesting the temperature propagation due to the second effect is limited. Therefore, only a small preserved domain is required, and the FMM-based simulation still offers significant acceleration with reasonable accuracy.

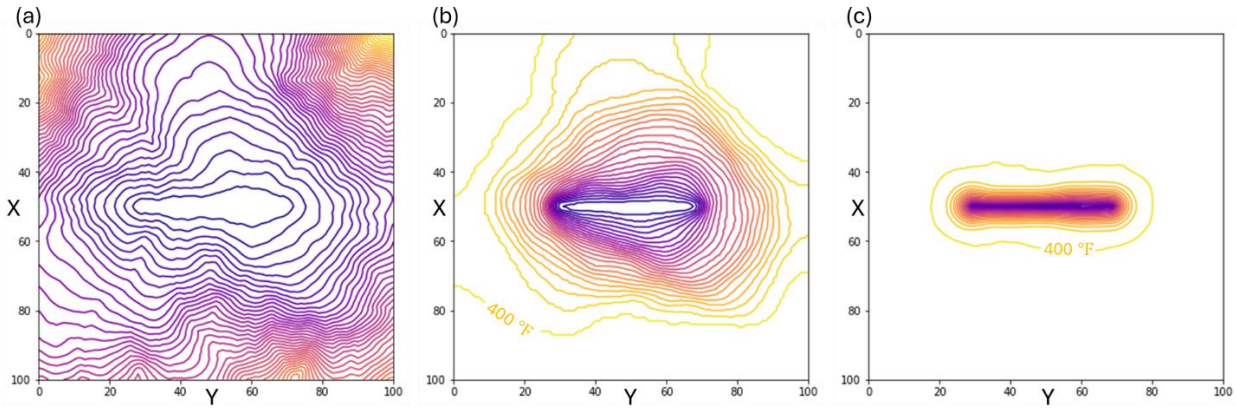

Figure A-1: Comparison of DTOF against two temperature distribution: (a) DTOF contours, (b) temperature distribution contours in production scenario, and (c) temperature distribution contours in injection scenario.